Mastering a 1.2 K hysteresis for martensitic para-ferromagnetic partial transformation in Ni-Mn(Cu)-Ga magnetocaloric material via binder jet 3D printing

Erica Stevens[a], Katerina Kimes[a], Daniel Salazar[b], Rafael Rodriguez[a], Aaron Acierno[a], Patricia Lázpita[b,c], Volodymyr Chernenko[b,c,d], Markus Chmielus[a]

……………………………………..

[a]Mechanical Engineering and Materials Science Department, University of Pittsburgh, Pittsburgh, PA, USA

[b]BCMaterials, Basque Center for Materials, Applications and Nanostructures, UPV/EHU Science Park, 48940 Leioa, Spain

[c]University of the Basque Country (UPV/EHU), Bilbao 48080, Spain

[d]Ikerbasque, Basque Foundation for Science, Bilbao 48013, Spain

Abstract

Magnetocaloric (MC) materials have gained traction in the research and industry communities for their prospects in solid state magnetic refrigeration. Important to the commercialization of MC materials are: (1) establishment of a fabrication method that can combine high surface area for heat transfer and geometric freedom for designing an efficient heat exchanger which has low pressure drop for the coolant and (2) advancement of low cost alloys with appropriate MC properties. In this regard, additive manufacturing may provide the geometric freedom necessary for adapting designs to solid state cooling, and the Ni-Mn(Cu)-Ga Heusler ferromagnetic shape memory alloys (FSMAs), exhibiting a martensitic para-ferromagnetic transformation at T_{ms}=304 K, can provide a low-cost MC material, very promising for magnetic cooling. In this study, a $Ni_{49.5}Mn_{19.1}Cu_{6.6}Ga_{24.8}$ (at.%) alloy is additively manufactured using powder bed binder jet 3D printing with subsequent sintering. This printed and sintered material enabled a large change of magnetization during partial transformation cycles with the smallest temperature hysteresis recorded for FSMAs, equal to about 1.2 K, regardless the value of magnetic field applied. Under 2 T and at 304 K it exhibits an adiabatic temperature change (ΔT_{ad}) of 2 K and a stable cycling behavior of $\Delta T_{ad} = |1.7|$ K for 100 cycles. The maximum of magnetic field-induced entropy change $|\Delta S_{\mathrm{m,\,2T}}| \approx 12.0$ J/kg·K was estimated at 304 K. These results demonstrate the viability of powder bed binder jet 3D printing as an effective fabrication method for functional magnetocalorics, as well as the outstanding MC characteristics of a low-cost Ni-Mn(Cu)-Ga Heusler-type FSMA.

Keywords

magnetic shape memory alloy, additive manufacturing, martensitic transformation, sintering, binder jetting, powder bed

1. Introduction

Worldwide energy consumption is increasing, and a large portion of this growth is generated by cooling technologies such as refrigerators and air conditioners [1]. Currently, refrigeration is produced through a vapor-compression cycle technology that has a maximum Carnot efficiency of 30-40%, can be loud, and uses chlorofluorocarbons (CFC's) and hydrochlorofluorocarbons (HCFC's), hazardous gases which contribute to ozone depletion [2,3]. Recently, the possibility of using solid state magnetic refrigeration, based on the magnetocaloric effect (MCE), has been proposed as an alternative technology. Magnetic refrigeration presents several advantages compared to the vapor-compression cycle: it can be 20-30% more efficient than the current technology, it is nearly silent because of the limited need for moving parts like the compressor in a typical system, and it is eco-friendly [2]. Nevertheless, many of the established MCE materials contain rare earth elements, such as Gd and La, which are economically strategic materials, and also present potential health risks to populations near to their mining sites and other occupational exposures [4,5].

Recently, two categories of the rare-earth-free Ni-Mn-based (In, Sn, Sb, Ga) Heusler-type magnetic shape memory alloys (SMAs), exhibiting a giant MCE due to the first order martensitic transformation (MT) near room temperature, have been researched: Mn-rich Ni-Mn-(In, Sn, Sb) metamagnetic SMAs (MetaMSMA) [6–9] and Ni-Mn-Ga ferromagnetic SMAs (FSMAs) [10]. MetaMSMA displays a large drop of its magnetisation (ΔM) in the temperature range of MT from the high-temperature ferromagnetic austenite to the low-temperature antiferromagnetic martensite, whereas in FSMA the large drop of ΔM is obtained as a result of MT from the ferromagnetic martensite to the paramagnetic austenite. The adiabatically applied magnetic field induces these magnetostructural transformations producing cooling of MetaMSMA, as a result of inverse MCE, and heating in the case of FSMA resulting from a conventional MCE. The large values of the field-induced isothermal entropy change (ΔS_m) and corresponding adiabatic temperature change (ΔT_{ad}) are the main parameters characterizing the MCE.

On the other hand, the typically large thermal hysteresis of MT (around 10 K) is a serious disadvantage of these materials since a very high magnetic field is required to achieve reversibility of a magnetostructural transformation [11–13]. Therefore, an important research goal to make these materials competitive is a narrowing of the thermal hysteresis of MT, which can be achieved primarily by tuning compositions. The other possible method, still not explored extensively in literature, is the exploration of partial transformations that can increase reversibility and decrease hysteresis [14].

Numerous sources compiling the current state of magnetocaloric cooling assert the need for a thermally efficient heat exchanger that has a high surface-to-volume ratio, in order to maximize heat transfer capabilities [13,15–17]. Such a heat exchanger is a challenge when fabrication or assembly techniques affect materials' functionality, leaving some alloys that show promise in laboratory testing to exhibit only a modest MCE after fabrication [18,19]. Currently, some of the attempted fabrication routes for magnetocaloric heat exchangers are: selective laser melting [18], powder packed bed [20], composite compaction [21], or polymer bonding [19,22]; each method has some limited success but none of them has emerged as the sole solution to the fabrication question. Typically, Ni-Mn-based Heusler MSMAs are manufactured as single crystals, thin films, foams, and polycrystals. Additive manufacturing (AM) can add the great possibility of fabricating complex shapes with controlled, designed porosity as explored through binder jet printing and laser-based manufacturing. Research studies in the area of additively manufactured MCE materials are sparse. Moore et al. studied the selective laser melting of magnetocaloric alloy $La(Fe, Co, Si)_{13}$ through comparison of two different bulk geometries [18]. Laser powder bed fusion of Ni-Mn-Ga is described in the recent work by Laitinen at al. [23,24] and Nilsen et al. [25]. Mostafaei et al. and Caputo et al. studied binder jet 3D printing of Ni-Mn-Ga with compositions more suitable for purposes of the magnetic shape memory actuators than for potential magnetocaloric applications [26–29]. Taylor et al. reported on the sintering of particle-based ink 3D printed elemental Ni, Mn, and Ga powder particle-containing inks [30]. Stevens et al. have introduced both direct laser deposition of Ni-Mn-Co-Sn MetaMSMAs and preliminary binder jet printing results for Ni-Mn(Cu)-Ga FSMA [31,32].

The present study explores a magnetocaloric material fabricated via binder jet 3D printing (BJ3DP), focusing on the Ni-Mn(Cu)-Ga FSMA, transforming martensitically near room temperature from the paramagnetic austenite into the ferromagnetic martensite. We found that the MT in this material can be realized with an extremely narrow thermal hysteresis of 1.2 K through a partial transformation still involving large values of ΔM, ΔS_m and ΔT_{ad}. The relatively small values of both hysteresis and transformation interval gave rise to the stable cycling amplitude of ΔT_{ad} to be equal to about 2 K under 2 T at 304 K.

2. Materials and methods

Eight polycrystalline ingots with a nominal composition of $Ni_{50.00}Mn_{18.75}Cu_{6.25}Ga_{25.00}$ (at.%) were prepared by induction melting from high purity (99.99+ %) elemental Ni, Mn, Ga, and Cu in an argon atmosphere. As-cast ingots were ball milled and sieved to particle sizes below 106 μm. Approximately 300 g of powder was used to fabricate cylindrical (5 mm height and 10 mm diameter) coupons via the BJ3DP additive manufacturing method on an ExOne X-1 Lab printer, using ExOne Solvent Binder 04. For printing the following parameter values were used: layer height 100 μm, spread speed 20 mm/s, feed/build powder ratio of 2, drying time 40 s, and binder saturation 80%. In the manufacturing process, a layer of powder is spread in a powder bed and flattened by a roller, then a printhead deposits binder selectively to adhere the powder within a single layer according to a 3D computer model. After each layer fabrication, a heater dries the binder and the powder bed lowers by the height of the layer. The process repeats until the desired part is completed. In post-processing, the BJ3DP workpieces were cured for 8 h at 473 K then de-powdered and densified via pressureless sintering. In this study, sintering was carried out in an encapsulated quartz tube with an argon-purged vacuum atmosphere and a Ti oxygen-getter, with a 5 K/min ramp to 1353 K, 2 h hold time, and air cool.

The microstructure at room temperature was analyzed with a Zeiss Sigma 500 FESEM equipped with EDS and a Zeiss Smartzoom 5 digital optical microscope (OM). Scanning electron microscopy (SEM) samples were prepared by cutting the sintered coupon in half with a wire saw, cold mounting, and standard metallographic polishing ending with an acidic alumina final polish. Table 1 shows the ingot nominal and average measured composition together with the final composition of the matrix of the printed workpiece including standard deviations. The ingot average refers to an average across the 8 ingots calculated from semi-quantitative EDS data obtained from area scans on each ingot, and workpiece matrix shows the same EDS data disregarding carbon. The differences between the nominal composition and the measured one for the workpiece are smaller than 1 at.% indicating that it was hardly affected by the fabrication process. A constant electronic concentration (*e/a*) value of 7.75 was observed in both the nominal and workpiece, thus indicating that similar structure, MT, and magnetic properties, implying similar functionalities to the corresponding alloys' homologues [33,34].

Table 1. Nominal, ingot average, and BJ3DP workpiece compositions with ± values representing standard deviation across all measurements. Ingot average refers to an estimate calculated from EDS data obtained from each ingot. EDS data for the BJ3DP workpiece are evaluated excluding carbon.

Composition, at.%	**Ni**	**Mn**	**Cu**	**Ga**
Nominal	50.00	18.75	6.25	25.00
Ingot average	48.5 ± 1.4	17.8 ± 0.4	8.0± 0.9	25.7 ± 1.0
BJ3DP workpiece	49.5 ± 0.3	19.1 ± 0.1	6.6 ± 0.2	24.8 ± 0.2

Porosity was determined with several methods, described elsewhere [26,35]. To this end, the workpiece density was measured by three different techniques: (i) Archimedes method with true density calculated through assumption of single martensitic phase (in contrast with previous publications using weighted molar masses [35,36]), (ii) micro-computed X-ray tomography (Bruker Skyscan 1272, 100 V, 100 μA, 0.11 mm Cu filter), and (iii) image analysis via ImageJ software [37].

Characteristic MT temperatures were determined by differential scanning calorimetry using a Pyris 6 DSC with a cooling/heating rate of 5 K/min.

Crystal structure and cell parameters were studied by X-ray diffraction (XRD) in a Bruker D8 XRD with Cu Kα radiation. For these experiments a rectangular prism (1.84 x 1.84 x 4.14 mm^3) was cut from the center of the initial workpiece. Diffraction patterns corresponding to a majority martensitic phase were recorded at room temperature. Analysis of XRD patterns was performed using the FullProf software [38].

Magnetic measurements were performed in a Quantum Design Superconducting Quantum Interference Device (SQUID) between 250 K and 340 K under applied magnetic fields up to 7 T. The $\mu_0 H$-T phase diagram was obtained from the analysis of the thermomagnetization curves. The indirect MCE was calculated from the series of isothermal *M*(*H*) curves using the Maxwell relationship [2,10]:

$$\Delta S_m(T,H) = S_m(T,H) - S_m(T,0) = \int_0^H \frac{\partial \mu_0 M(T,H')}{\partial T} \mathrm{d}H' \qquad (1)$$

To avoid an influence of a partial transformation induced by magnetic field, the sample was heated each time above the austenite finish temperature before being zero-field cooled (ZFC) down to the testing temperature [39]. Direct MCE measurements were carried out on cooling and under an applied magnetic field of 1.96 T (hereafter rounded to 2 T) in an custom-built adiabatic calorimeter as described in [40]. As in the case of the *M*(*H*) curves, before each measurement, the sample was heated above the austenite finish temperature to mitigate residual effects. It must be emphasized that the thermocouples used in different instruments have different sensitivities and calibrations, causing the temperature readings to be inherently inconsistent across techniques. Thermocouple positions also vary, from measuring while in contact with the sample to measuring the air near the sample. Therefore, during analysis, the thermomagnetization curves were shifted by a few degrees along the temperature axis to achieve a congruency with the other results. Note, small slices of different weights (2-100 mg), depending on the test's specific required dimensions, were cut out from the same workpiece material to serve as the samples for XRD, DSC, magnetic and MCE measurements.

3. Results

3.1. Microstructure

The results of density analysis are shown in Table 2. It is worth noting that the evaluation region for each technique was different. Archimedes method measured the bulk density (94% ± 1 pp [percentage points]). Micro-computed X-ray tomography (μCT) is only successful on small samples, so a sliver was cut from near the center of the workpiece (96% ± 1 pp). The image analysis was performed on micrographs from the sample after it was cut in a half near the center, so is more representative of a central plane (92% ± 1 pp). For Archimedes and μCT results, the error is directly related to the measurements, while for image analysis it is the standard deviation from 4 images. The backscattered electron micrographs in Figure 1 show that the pore distribution is common for a part sintered from powder. Pores are located along grain boundaries and are generally larger near the edges of the part.

Table 2. Densities of BJ3DP sample measured using Archimedes, μCT, and imaging methods. Error for Archimedes and μCT is measurement-related, and for OM image analysis it is a standard deviation. Measured area or volume is also listed.

	Archimedes	μCT	Imaging
Density	94%	96%	92%
Error	± 1 pp	± 1 pp	± 1 pp
Measured	Bulk	Center Sliver	Center

As anticipated for binder jet printing with the subsequent sintering at a sub-solidus temperature (no melting was involved), a homogeneous microstructure regarding the grain size and dominant phase, as well as the equilibrium shape of grains are evident in Figure 1. Grain size was measured from 82 grains in optical micrographs to be 130 ± 30 μm in circle-equivalent diameters, slightly larger than the feedstock powder size due to coarsening during sintering. Figure 1 also shows that the grains consist of twins with the differently oriented twin boundaries, indicating a dominant presence of the martensite phase at room temperature.

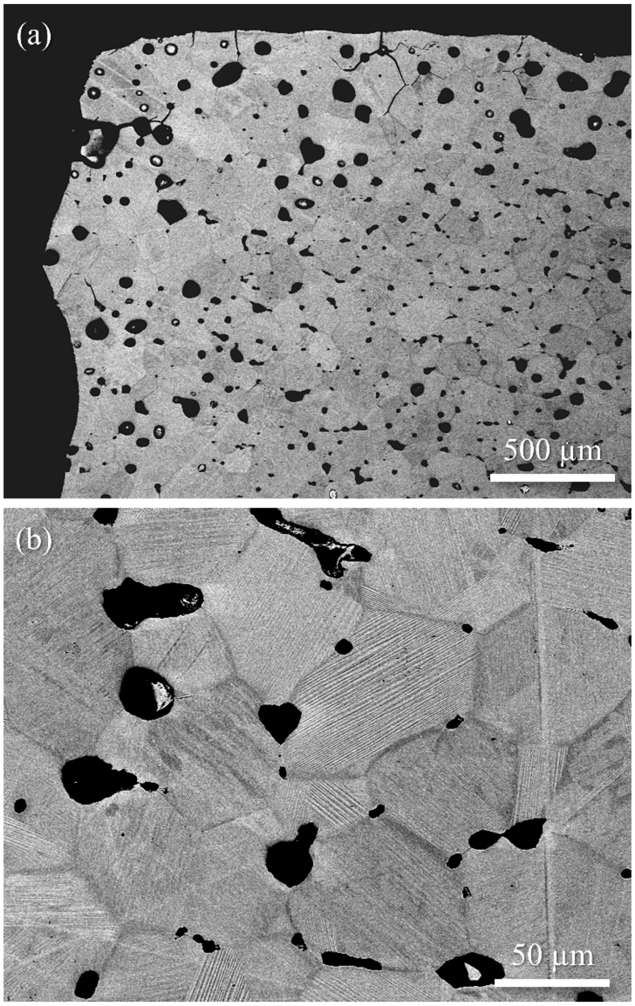

Figure 1. Backscattered electron micrographs of a polished cross section of the BJ3DP part. (a) An overview of a corner of the part; and (b) a magnified view of pores along grain boundaries and grains exhibiting twinned martensitic phase.

µCT-collected radiographs and subsequently reconstructed 2D slices were used to generate both porosity data and 3D visualizations. Figure 2 and the supplementary video corroborate 2D porosity and grain information. Particularly, Figure 2 shows a single grain with porosity along the grain boundary. This figure also confirms the existence of both standalone spherical pores and connected porosity, signifying that sintering progressed to the intermediate stage [41,42]. In a µCT-reconstructed analyzed volume of 0.3 mm^3, the part had an average structure separation of 22 ± 12 µm, and an average structure thickness of 92 ± 24 µm. Within the same volume, pores had a median sphericity of 0.78, with 66% of pores having sphericity > 0.7 and 45% of pores having a sphericity > 0.8.

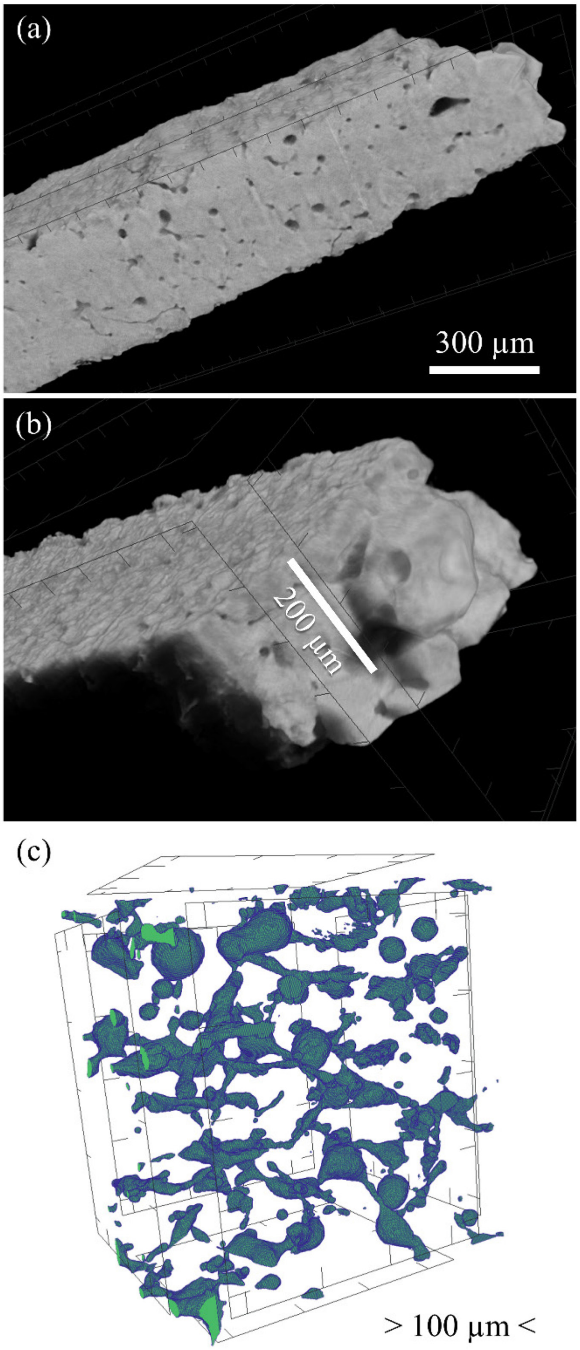

Figure 2. 3D visualizations using data collected by µCT. (a) The view of a cut side of the slice, (b) a single grain on the top of the slice, and (c) porosity only, visualized for a small cube of volume.

3.2. Martensitic transformation and crystal structure

Figure 3 displays DSC curves, where the reverse and forward MTs on heating and cooling are accompanied by sharp endothermic and exothermic peaks, respectively. DSC scans were measured up to 428 K (not shown here) to confirm that no additional transformations occur in the material. The characteristic temperatures of MT, martensite start (M_s), martensite finish (M_f), austenite start (A_s), and austenite finish (A_f), have been estimated from DSC curves using the two-tangent intersection method, and they are summarized in Table 3. The MT temperatures of the forward and reverse transformations have been defined as $T_M = (M_s + M_f)/2$ and $T_A = (A_s + A_f)/2$, respectively, being $T_M = 299$ K and $T_A = 306$ K. The MT hysteresis is equal to $\Delta T_\mathrm{h} = T_A - T_M = 7$ K. For comparison, Table 3 also contains the MT data derived from the magnetization measurements discussed in Section 3.3.

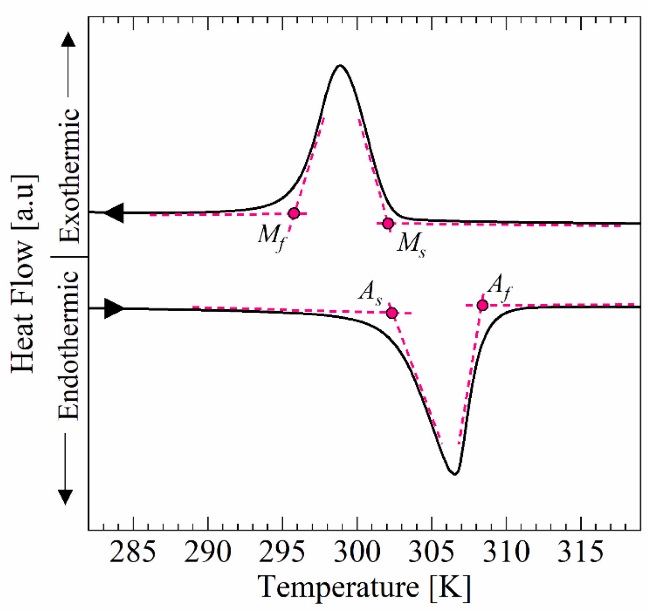

Figure 3. Calorimetric curves showing the reverse and forward martensitic transformation during heating and cooling, respectively. Two-tangent method intersection points are drawn to indicate the locations of martensite start (M_s), martensite finish (M_f), austenite start (A_s), and austenite finish (A_f) temperatures.

Table 3. Characteristic temperatures of MT determined from DSC scans and from thermomagnetization curves measured under different magnetic fields.

	Field [T]	M_s [K]	M_f [K]	T_M [K]	A_s [K]	A_f [K]	T_A [K]
DSC	0.00	302	296	299	303	309	306
SQUID*	0.01	303	298	300	303	307	305
	0.10	303	301	302	305	308	306
	1.00	305	302	304	306	309	308
	3.00	307	305	306	309	312	310

7.00	311	309	310	312	315	314

*See Section 3.3 for details

The experimental and calculated XRD patterns are shown in Figure 4. At 300 K, they present a non-modulated tetragonal martensite (NM martensite) with the presence of some amount of the residual austenite. Table 4 summarizes the unit cell parameters determined for the martensitic and austenitic phases.

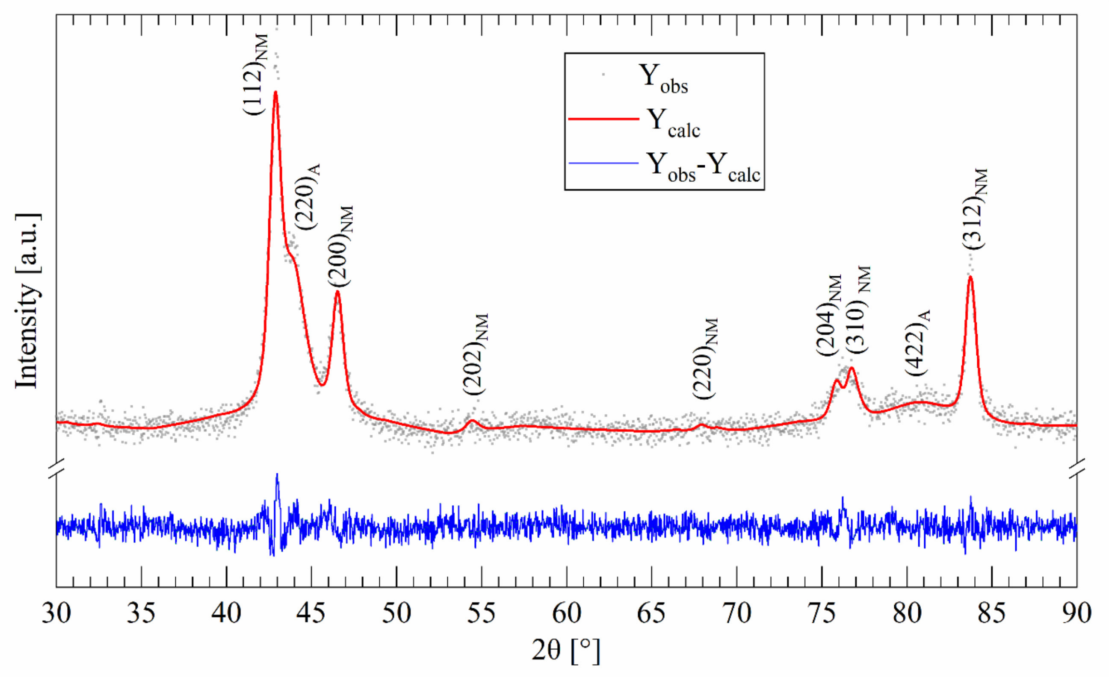

Figure 4. The experimental and calculated XRD patterns representing the two-phase state at T = 300 K. Indexing is according to the non-modulated tetragonal structure of martensite, NM (space group I4/mmm) and cubic $L2_1$-ordered austenite, A (space group Fm-3m).

The values of parameters in Table 4 are in good agreement with the literature. Li et al. reported the $L2_1$ phase in $Ni_{44}Cu_6Mn_{31}Ga_{19}$ to have a_0 = 5.865 Å [43], larger than the values reported here due to the higher amount of Mn, which has the largest atomic radius of the contained non-doping elements. Sarkar et al. reported lattice parameters of the $L2_1$ phase in $Ni_{50}Cu_{6.5}Mn_{18.5}Ga_{25}$ to have a_0 = 5.802 Å and the I4/mmm NM phase for $Ni_{50}Cu_7Mn_{18}Ga_{25}$ to have a = 3.893 Å and c = 6.436 Å [44], and again a difference in Mn concentration could cause this mismatch. The nearest composition of $Ni_{50}Cu_{6.25}Mn_{18.75}Ga_{25}$ was reported by Roy et al. to have an $L2_1$ lattice parameter of a_0 = 5.814 Å [45].

Table 4. Unit cell parameters determined for non-modulated tetragonal martensite (space group I4/mmm) and austenite (space group Fm-3m)

	Martensite	Austenite
Lattice parameters	NM tetragonal	$L2_1$ cubic
a [Å]	3.903	a_0=5.830
c [Å]	6.547	

3.3. Magnetization behavior

The results of thermomagnetization measurements performed at constant magnetic fields are depicted in Figure 5(a). They show only one hysteretic anomaly, which means that the ferromagnetic order appears when the forward MT proceeds. The obtained $M(T)$ loops in Figure 5(a) were collected between full martensitic phase (low temperature) and full austenitic phase (high temperature). During the heating process there is a large drop in magnetization corresponding to the reverse MT from a ferromagnetic martensitic to a paramagnetic austenitic phase. The transformation is fully reversible during cooling - heating cycles. Under the influence of a magnetic field, the MT shifts to higher temperatures due to the stabilization of the ferromagnetic martensitic phase. Table 3 collects the MT characteristic temperatures obtained by the two-tangent method using data from Figure 5(a).

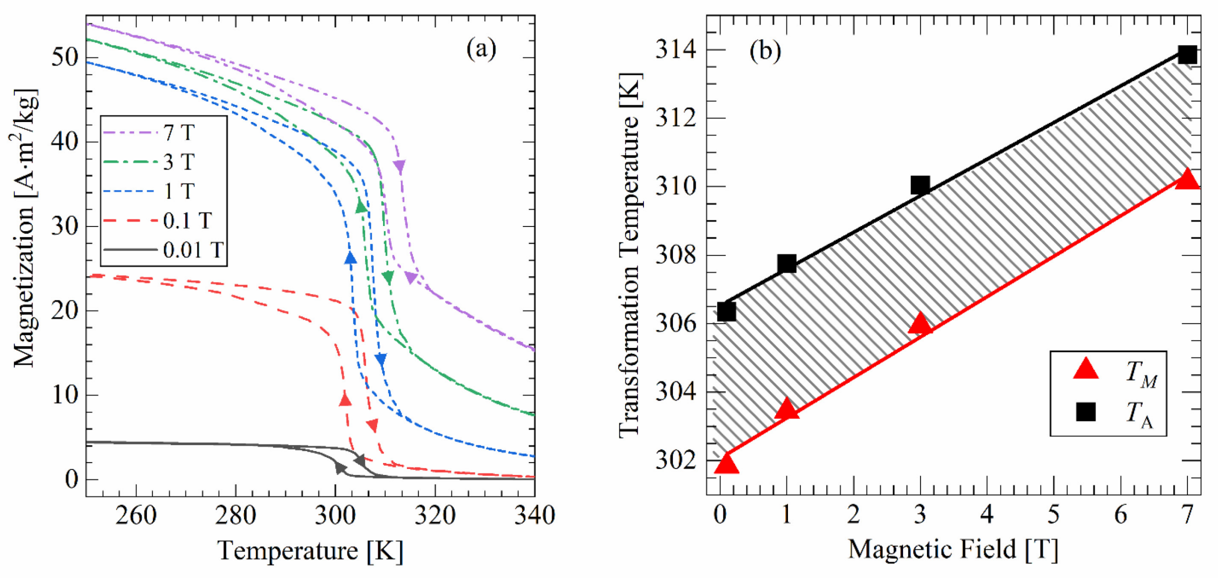

Figure 5. (a) Magnetization versus temperature dependencies during cooling-heating ramps in various fields. (b) $\mu_0 H$-T phase diagram of the magnetostructural transformation, showing MT hysteresis almost independent of the magnetic field.

The MT temperatures are plotted in Figure 5(b) as a function of the magnetic field, thereby representing a $\mu_0 H$-T phase diagram, approximated by linear dependencies with almost the same slope, equal to $dT_M/d\mu_0 H = 1.2 \pm 0.1$ K/T. The shaded area in Figure 5(b) corresponds to the quasi-stable presence of martensitic or austenitic phase within a hysteresis loop, depending on whether heating or cooling is performed, respectively.

In the present work, we found that a drastic decrease of the MT hysteresis can be achieved by partial cycling through the thermally- or magnetic field-induced MT, where only some fraction of material is reversibly transforming. Figure 6 shows the measured partial *M*(*T*) hysteresis loops which exhibit a thermal hysteresis equal to 1.2 ± 0.1 K for the largest partial loop at all applied fields (the value of hysteresis was taken as a temperature difference of averaged transformation temperatures found using the two-tangent method for the forward and reverse MT). It will be shown below that with such a record-breaking value of hysteresis, the practically important MCE parameters of Ni-Mn-Ga-type FSMA can be obtained, since not only thermal hysteresis, but also a large value of ΔM and a relatively narrow MT interval can be involved in partial cycling. The behavior of the last two parameters can be appreciated from Figure 6(a) and for comparison sake with the complete MT cycles in Figure 6(b). Magnet designs for magnetic refrigeration reach magnetic field values of not more than 2 T [46,47], the reason that detailed *M*(*H*) measurements were carried out up to 2 T only.

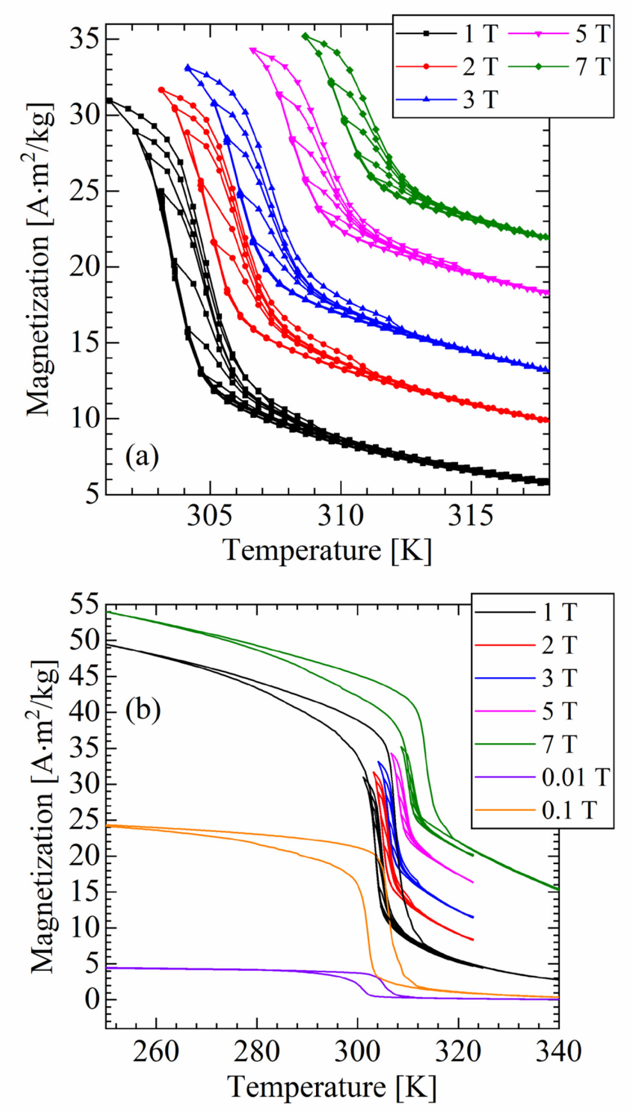

Figure 6. (a) Thermomagnetization curves at different magnetic fields recorded during cycling across thermally induced partial MT; (b) overlapping of several graphs from Figure 5(a) with the partial *M*(*T*) cycling depicted in Figure 6(a) to highlight a drastic reduction of the thermal hysteresis while maintaining large values of magnetization drops.

Isothermal *M*(*H*) curves measured in the vicinity of MT in the steps of 0.5 K are plotted in Figure 7. Before each measurement, the sample was heated to austenite and returned to the measuring temperature in order to avoid any influence of the partial transformation induced by the magnetic field. For the sake of clarity, only the curves recorded during increasing of magnetic field are displayed in Figure 7. To demonstrate magnetic field-induced reversibility of MT, two complete *M*(*H*) loops are shown in the inset, as an example. At low temperature (301 K), the martensitic phase shows a regular ferromagnetic behavior, although it is not saturated even at 2 T. At high temperature (308 K) the magnetization is strongly reduced. It exhibits a nonlinear dependence due to the presence of two phases at this temperature: the ferromagnetic martensitic phase and paramagnetic austenite with a domination of the latter phase. For the intermediate temperatures, the non-regular change of the susceptibility is related to the magnetic field induced partial MT.

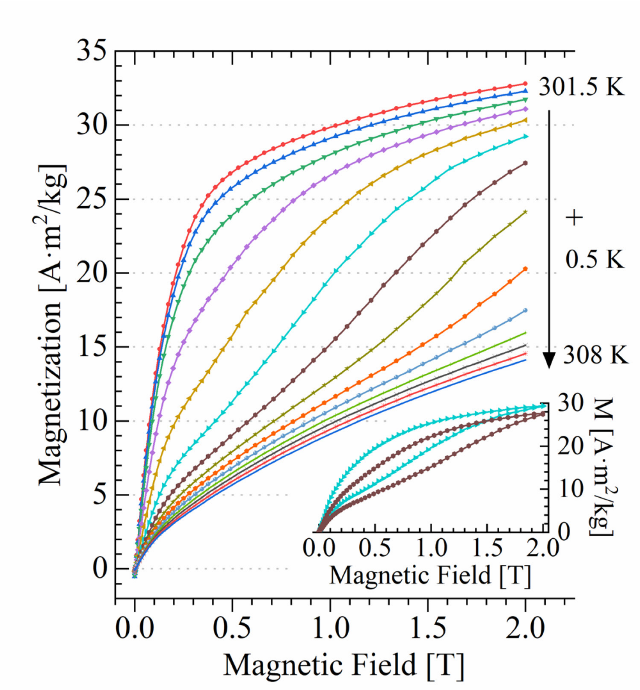

Figure 7. Isothermal *M*(*H*) curves, taken at each of the 0.5 K increments from 301.5 K to 308.0 K. Inset shows an exemplary full loop reversal behavior for 304 K (light blue) and 304.5 K (brown).

3.4. Adiabatic magnetocaloric response

The conventional MCE, which should occur in the studied alloy at its magnetostructural transformation, was characterized by the indirect (evaluation of ΔS_m) and the direct (measurements of ΔT_{ad}) methods. The $\Delta S_m(T)$ dependences were calculated from the isothermal *M*(*H*) curves in

Figure 7 using the Maxwell relationship, Eq.(1), and the results are given in Figure 8 for different applied magnetic field changes. All the curves present a high and narrow minimum, resulting from the field induced change of magnetic order. This change is related to the partial or full occurrence of the forward MT from the low-magnetization paramagnetic austenitic phase to the high magnetization ferromagnetic martensitic one. The maximum value of $|\mathit{\Delta} S_{m,\,2\mathrm{T}}|$ is equal to ≈12.0 J/kg·K.

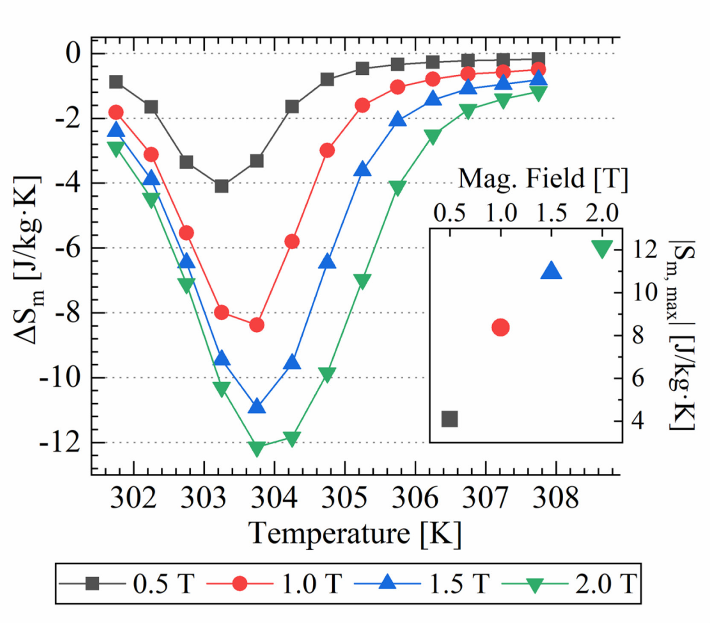

Figure 8. Temperature dependencies of the magnetic field induced entropy change, $\mathit{\Delta} S_m$, at different constant magnetic fields in the range from 0.5 T to 2.0 T, calculated using isothermal magnetization data in Figure 7. Inset demonstrates the evolution of $\mathit{\Delta} S_{m,\,max}(H)$

The adiabatic MCE response was measured during step-like cooling upon sample insertion into the magnetic fields of 1 T and 2 T in adiabatic conditions. The same procedure was followed as in the case of the isothermal $M(H)$ measurements, i.e., before each temperature test the sample was heated to full austenite and then the temperature was slowly reduced to the target temperature. The results are depicted in Figure 9. The maximum temperature change, $\Delta T_{\mathrm{ad}} = 2.0 \pm 0.1$ K, at 2 T, was obtained at T_{M}. The peak on the curve $\Delta T_{\mathrm{ad}}(T)$ spans approximately 10 K. For lower applied magnetic fields, the ΔT_{ad} is reduced; a 50% reduction of the applied field results in a corresponding decrease in MCE response to about 1 K.

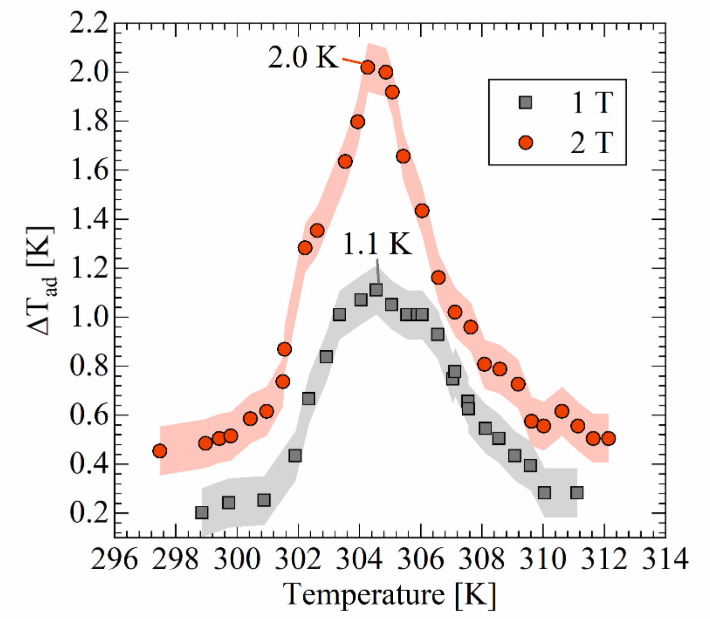

Figure 9. Magnetic field induced adiabatic temperature change at 1 T and 2 T measured at different temperatures during step-like cooling. Shaded bands indicate a ±0.1 K of uncertainty in the measurements.

Cycling measurements of ΔT_{ad} were conducted at constant temperatures by inserting/removing the sample into/from the magnetic field of 2 T with a full cycle time of 10 s. Variations in the temperature baseline are due to the imperfect manual control of the temperature via air flow regulation, but slow varied fluctuations were limited to within 0.5 K. Results of measurements close to T_M are shown in Figure 10. Figure 10(a) presents the entire 101 measured cycles at a nominal temperature of 304 K. Figure 10(b) is a rescaled view of what a series of measurements looks like and is extracted directly from the data in Figure 10(a). Shown in the box in Figure 10(c), a single measurement consists of a cluster of the data points collected when the sample is in a 0 T magnetic field and when it heats up under 2 T. The difference between the lower- and higher-temperature clusters of data points is the measured ΔT_{ad}.

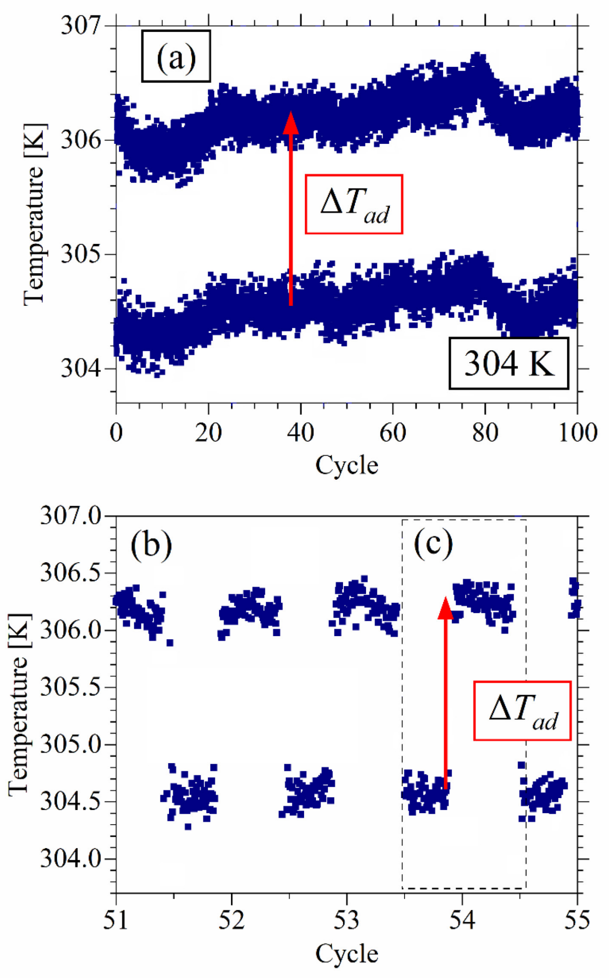

Figure 10. Adiabatic temperature change of the sample under the magnetic field on/off cycling conducted at 304 K. (a) Results for 101 cycles. (b) Rescaled view of several measurement cycles showing the step-like change of the temperature of the sample induced by its periodic inserting/extracting into/from the magnetic field of an electromagnet. (c) A single measurement, indicating the value of ΔT_{ad}.

Figure 11 shows the stability of ΔT_{ad} during cycling measurements. At the temperature where ΔT_{max} was observed (304 K), the sample was repeatedly inserted into and removed from the field. The first cycle showed the highest value of 1.95 K, near that observed in the initial direct MCE response test. Past the first point, ΔT_{ad} dropped to approximately 1.65 K, with 97.5% of the 100 cycles and their ±0.5 K error bars falling within 1.55-1.75 K. The appearance of a slight trend upwards is because of the slight upward trend in manually controlled temperature, which can be seen in Figure 10(a).

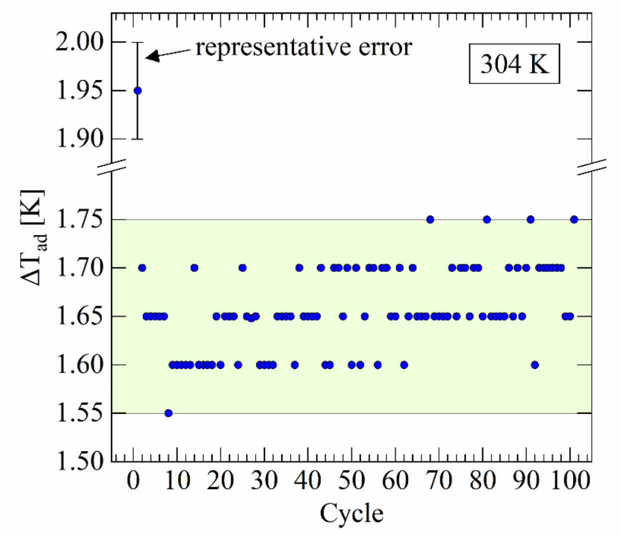

Figure 11. Magnetic field cycling performed at the temperature where ΔT_{max} was observed (304 K). The first data point shows a representative ±0.5 K of uncertainty that is assumed to be valid for all other plotted points. The filled area indicates where 97.5% of all points and their error bars fall within, excluding the first data point.

4. Discussion

4.1. Analysis of transformation characteristics

Table 5 compiles the data obtained in the present work and compared to literature for similar FSMAs. For convenience of comparison, the compositions for all alloys are presented as the chemical formula. Table 5 shows the slight increased value of the unit cell volume of martensitic phase calculated for BJ3PD sample, 99.73 $Å^3$, compared to that calculated using data presented by Sarkar et al. [44], 97.54 $Å^3$, or from Wroblewski et al. [48], 96.64 $Å^3$. These variations can be related to the differences in the composition. Also, an influence of the possible antisite atomic disorder and/or interstitial positions of some atoms (possibly carbon) could not be discarded.

A minimized temperature hysteresis of the magnetostructural transformation is extremely necessary for the long-life cycling stability of MCE material. Table 5 shows that, whereas the characteristic transformation temperatures of the BJ3DP alloy and materials prepared by conventional methods all have $T_{\max}$ close to room temperature, the thermal hysteresis of the complete MT, ΔT_{h}, appears reduced, from the lowest values 9-11 K [44,49,50] to about 7 K in the printed sample. Different rationales can justify this reduction. For instance, the porosity and large grain size may be factors favoring a low hysteresis. Studies on nonmagnetic Cu-based SMAs show that the hysteresis is reduced as the grain size grows, reaching a minimum for grain size higher than 100 μm [51]. In our case, the high temperature sintering process increases the grain size in BJ3DP sample which can result in the reduction of ΔT_{h}. Furthermore, the width of thermal hysteresis exhibited by the thermoelastic MT is directly proportional to the residual stress (low thermal hysteresis for low residual stress) [52]. Residual stresses are minimal in BJ3DP parts because the printing process does not introduce any sharp thermal gradients through heating-cooling cycles, as selective laser melting does [53]. All of these factors can contribute to a reduction of ΔT_{h}. Thus, the above discussion indicates that the AM fabrication process does not have a significant impact on composition, structure or characteristic temperatures, but reduces the width of the main hysteresis loop characterizing the complete MT.

Naturally, the hysteresis loop of the partial MT should be located inside of the main MT loop, whereby the further reduction of hysteresis width is expected. It is very hard to predict the width of partial hysteresis since the theoretical description must deal with the processes of the volume fraction evolution in the locally nonequilibrium two-phase states [54]. In our work, we found experimentally that the Ni-Mn-Ga based material exhibits a partial MT accompanied by a more than 5 times reduced hysteresis if compared to the complete MT, Figure 6(b).

A reduction of MT hysteresis was also observed for Ni-Mn-In(-Co) metamagnetic shape memory alloy (MMSMA) when partial cycles were performed starting from the martensitic phase [7,8]. While the hysteresis reduction in [7,8] is much smaller than that observed here, this can be explained by the radically different interplay between mechanisms contributing to the energy barrier for phase transformation: phase stabilization with field applied, stress buildup at the habit plane and during reorientation of twin variants, formation of nucleation centers, and reduction of stress fields by way of open surfaces. In Ni-Mn-In(-Co) MMSMA, the field-preferred phase is austenitic. Gottschall et al. point out that in partial cycles (minor loops) from low temperatures, energy is saved through preserving martensitic nucleation sites [8] and they additionally propose that there is a buildup of stresses as twin variants reorient in the two-phase region [7]. Both preservation of martensitic nucleation sites and stress buildup during twin variant reorientation shift MT to lower temperatures and encourage transition to the high-temperature austenitic phase. Alternatively, in the case of the studied printed and porous Ni-Mn(Cu)-Ga FSMA, the field-preferred phase is martensitic. Though stress fields form at the habit planes, stress relief and easy nucleation can occur at the porosity concentrated at grain boundaries. Therefore, although energy is required for the martensitic nucleation centers to form, it is clearly outweighed by the energy savings due to a preferred martensitic phase and porosity resulting in stress relief and easy nucleation sites. An appearance and relaxation of mechanical stresses during partial or complete MT can be monitored by the diffraction methods at large-scale facilities (see, e.g., [55,56]).

4.2. Magnetocaloric effect and technological issues

The direct MCE measurements show ΔT_{max} of 2.0 K at 2 T for the first test, and a stable field-induced temperature change of approximately 1.65 K for 100 cycles more. The first cycle normally results in a higher measured effect, but during achieving its stability while cycling, the signal is expected to be reduced. The value of the decrease depends on the amount of residual phases during the partial martensitic transformation [9]. Following [8], the changes of magnetization caused by the complete and partial MT (see $M(T)$ curves in Figure 6(b)) were used for rough estimation of the volume fraction of the martensitic phase involved during sample cycling at 304 K under 2 T, equal to about 70%. Comparing with the other polycrystalline samples shown in Table 5, the similar MCE characteristics have been determined for similar composition, but one should bear in mind that no cycling experiments were previously performed in order to determine the value of stabilized ΔT_{ad}.

Contrary to the other studies, our MCE material was produced with binder introduced during the 3D printing phase, cured in an oven, and mostly burned out during sintering. However, sintering is conducted in argon-purged vacuum and in an enclosed quartz tube, not allowing for burnout products to be carried away. Because of this, the Ti sponge was placed as an oxygen getter. In addition to oxygen, the binder composition includes carbon, which cannot be as simply trapped by a getter. It is expected therefore, that carbon is trapped within the BJ3DP sample. Trapped carbon could be partially incorporated into a crystal lattice of FSMA as an interstitial, potentially causing some of the volumetric expansion observed over the data from Refs.[44,48], as indicated in Table 5. Though inclusions are often considered detrimental for the functional properties, an intentional hydrogenation of magnetocaloric material $La(Fe,Si)_{13}$, for instance, allows for tuning of MCE without precluding stability [57]. Carbon could serve a similar tuning purpose in binder jet 3D printed magnetocaloric materials, expanding the ranges of acceptable compositions and opening a new avenue for fabrication. This issue should be clarified in a separate investigation through a crystallographic study, i.e. by neutron diffraction experiments.

Table 5. Heat treatment at temperature (T_{an}) during time (t); martensitic start temperature (M_s); temperature hysteresis of MT (ΔT_h); unit cell volume of martensitic phase (V); and MCE characteristics ($|\Delta S_{m,\,max}|$, one-way ΔT_{ad}) obtained at T_{max} under applied magnetic field ($\mu_0 \Delta H_{app}$) for Ni-Mn(Cu)-Ga alloys exhibiting magnetostructural transformation. ~~Compositions are standardized by at.%/25.~~

Composition	**T_{an} [K]**	**t [h]**	**Cooling**	**M_s [K]**	**ΔT_h [K]**	**V [Å^3]**	**$\mu_0 \Delta H_{app}$ [T]**	**T_{max} [K]**	**$\lvert\Delta S_{m,\,max}\rvert$ [J/kg·K^{-1}]**	**$\Delta T_{ad,\,max}$ [K]**	**Ref.**
$Ni_{49.5}Mn_{19.1}Cu_{6.6}Ga_{24.8}$ (BJ3DP)	1353 (sinter)	2	air cool	302	7 (full)	99.80 (NM tetragonal)	2	304	12.1	2.0	This work
					1.2 (partial)	198.16 ($L2_1$ cubic)	2	304	-	1.7 (cyclic)	
$Ni_2Mn_{0.75}Cu_{0.25}Ga$	1073	144	furnace	308	-	-	2	308	28	-	[58]
$Ni_{49.89}Mn_{19.10}Cu_{6.43}Ga_{24.58}$	1123	24	-	289	10	195.31 ($L2_1$ cubic)	1	303	10.2	-	[44]
$Ni_{49.9}Mn_{19.6}Cu_{5.7}Ga_{24.8}$	-	-	furnace	290	-	96.64 (NM tetragonal)	2	300	9.86	0.23	[48]
$Ni_2Mn_{0.75}Cu_{0.25}Ga$	1073	144	furnace	308	-	-	2	303	-	1.5	[59]
$Ni_{49.3}Mn_{18.4}Cu_{7.6}Ga_{24.7}$	1173	24	-	316	11	-	1.5	321	12.8	1.6	[49]
$Ni_{50}Mn_{18}Cu_7Ga_{25}$	1173	24	air cool	314	9	-	2	~322	14.3	-	[50]

In addition to the possible incorporation of carbon, the influence of pores and grain boundaries merits further study as well. We found that along most of the grain boundaries several pores exist (Figures 1 and 2) as a result of incomplete densification. Some of the grain boundary pores have oxides of several microns diameter embedded, as previously shown in [32]. Small-scale (10 nm) matrix-dispersed Mn oxides have been identified in Ni-Mn-Ga thin films even after careful preparation and annealing in inert atmosphere [60–62]. Since surface and matrix-distributed Mn-O is unavoidable in these alloys, these are not expected to impact the comparison of MT values with other literature sources, which would experience the same. Mn-O particles found at the grain boundaries of the studied alloy in [32] may aid in inter-grain stress relief while not being detrimental to MT since they are not integrated into the matrix. For structural materials, porosity and grain boundary precipitates are detrimental, but in functional materials like Ni-Mn-Ga FSMAs, for which cyclic functionality depends upon both a reversible unit cell volume change and constraints at grain boundaries, porosity can be highly beneficial [63].

5. Conclusions

Additive manufacturing in the form of powder bed binder jet 3D printing is shown to be a viable method for producing magnetocaloric Ni-Mn(Cu)-Ga FSMAs. Post-processing included sintering in an argon-purged vacuum atmosphere followed by an air cool. Samples showed a ΔT_{ad} of 2 K under 2 T at 304 K. The subsequent cycling resulted in a stable ΔT_{ad} of approximately 1.65 K. The stable cycling of such a value of ΔT_{ad} is achieved owing to a record-breaking for FSMAs low hysteresis, of 1.2 K, accompanying a partial magnetostructural martensitic transformation, with still-high values of ΔM and a narrow transformation interval. The possible incorporation of carbon from the binder may cause observed volumetric expansion which might serve as additional factor improving functionality of printed material. Pores at grain boundaries allow for better conditions for reversible volumetric expansion necessary for functionality. Powder bed binder jet printing is proved to be a successful processing route for magnetocaloric materials, such as Ni-Mn-Cu-Ga FSMA.

Acknowledgements

This work was performed at the Nanoscale Fabrication and Characterization Facility, a laboratory of the Gertrude E. and John M. Petersen Institute of NanoScience and Engineering; at the Materials Micro-Characterization Laboratory containing the Fishione Center of Excellence for EM-sample Preparation; at the ANSYS Additive Manufacturing Research Laboratory; and at the Materials Characterization Laboratory housed within the University of Pittsburgh's Department of Chemistry. This project was supported in part by a fellowship award through the National Defense Science and Engineering Graduate (NDSEG) Fellowship Program, sponsored by the Air Force Research Laboratory (AFRL), the Office of Naval Research (ONR) and the Army Research Office (ARO). For partial funding KAK, ELS, RR, AA and MC would like to thank the Mascaro Center for Sustainable Innovation, University of Pittsburgh and the NSF [grant number 1727676 including an REU supplement]. This work was also carried out with the financial support of the Spanish Ministry of Science and Innovation (project RTI2018-094683-B-C53) and Basque Government Department of Education (project IT1245-19). Drs. J. Feuchtwanger and A. Perez Checa are acknowledged for technical assistance. A. Mostafaei is acknowledged for his help in an operating the ExOne X-1 Lab printer, J. Toman for his help regarding powder production, and E. Dickinson for her help automating temperature change measurement for cycling. The authors thank for technical and human support provided by SGIker (UPV/EHU/ ERDF, EU), especially Dr. Iñaki Orue, for the magnetization measurements.

References

[1] Commercial Buildings Energy Consumption Survey (CBECS), U.S. Energy Information Administration, (2013). http://www.eia.gov/consumption/commercial/reports/2012/energyusage/ (accessed January 15, 2017).

[2] J. Lyubina, Magnetocaloric materials for energy efficient cooling, J. Phys. D. Appl. Phys. 50 (2017) 053002. https://doi.org/10.1088/1361-6463/50/5/053002.

[3] M. Balli, S. Jandl, P. Fournier, A. Kedous-Lebouc, Advanced materials for magnetic cooling: Fundamentals and practical aspects, Appl. Phys. Rev. 4 (2017). https://doi.org/10.1063/1.4983612.

[4] G. Pagano, F. Aliberti, M. Guida, R. Oral, A. Siciliano, M. Trifuoggi, F. Tommasi, Rare earth elements in human and animal health: State of art and research priorities, Environ. Res. 142 (2015) 215–220. https://doi.org/10.1016/j.envres.2015.06.039.

[5] W. Gwenzi, L. Mangori, C. Danha, N. Chaukura, N. Dunjana, E. Sanganyado, Sources, behaviour, and environmental and human health risks of high-technology rare earth elements as emerging contaminants, Sci. Total Environ. 636 (2018) 299–313. https://doi.org/10.1016/j.scitotenv.2018.04.235.

[6] V.A. Chernenko, V.A. L'vov, E. Cesari, J.M. Barandiaran, Fundamentals of magnetocaloric effect in magnetic shape memory alloys, in: Handb. Magn. Mater., 1st ed., Elsevier B.V., 2019: pp. 1–45. https://doi.org/10.1016/bs.hmm.2019.03.001.

[7] T. Gottschall, K.P. Skokov, R. Burriel, O. Gutfleisch, On the S(T) diagram of magnetocaloric materials with first-order transition: Kinetic and cyclic effects of Heusler alloys, Acta Mater. 107 (2016) 1–8. https://doi.org/10.1016/j.actamat.2016.01.052.

[8] T. Gottschall, K.P. Skokov, B. Frincu, O. Gutfleisch, Large reversible magnetocaloric effect in Ni-Mn-In-Co, Appl. Phys. Lett. 106 (2015). https://doi.org/10.1063/1.4905371.

[9] J. Liu, T. Gottschall, K.P. Skokov, J.D. Moore, O. Gutfleisch, Giant magnetocaloric effect driven by structural transitions., Nat. Mater. 11 (2012) 620–6. https://doi.org/10.1038/nmat3334.

[10] C. Seguí, J. Torrens-Serra, E. Cesari, P. Lázpita, Optimizing the Caloric Properties of Cu-Doped Ni–Mn–Ga Alloys, Materials (Basel). 13 (2020) 419. https://doi.org/10.3390/ma13020419.

[11] V. Khovaylo, Inconvenient magnetocaloric effect in ferromagnetic shape memory alloys, J. Alloys Compd. 577 (2013) S362–S366. https://doi.org/10.1016/j.jallcom.2012.03.035.

[12] V. Franco, J.S. Blázquez, J.J. Ipus, J.Y. Law, L.M. Moreno-Ramírez, A. Conde, Magnetocaloric effect: From materials research to refrigeration devices, Prog. Mater. Sci. 93 (2018) 112–232. https://doi.org/10.1016/j.pmatsci.2017.10.005.

[13] O. Gutfleisch, T. Gottschall, M. Fries, D. Benke, I. Radulov, K.P. Skokov, H. Wende, M. Gruner, M. Acet, P. Entel, M. Farle, Mastering hysteresis in magnetocaloric materials, Philos. Trans. R. Soc. A Math. Phys. Eng. Sci. 374 (2016) 20150308. https://doi.org/10.1098/rsta.2015.0308.

[14] F. Guillou, H. Yibole, G. Porcari, L. Zhang, N.H. Van Dijk, E. Brück, Magnetocaloric

effect, cyclability and coefficient of refrigerant performance in the MnFe(P, Si, B) system, J. Appl. Phys. 116 (2014). https://doi.org/10.1063/1.4892406.

[15] S. Fähler, U.K. Rößler, O. Kastner, J. Eckert, G. Eggeler, H. Emmerich, P. Entel, S. Müller, E. Quandt, K. Albe, Caloric Effects in Ferroic Materials: New Concepts for Cooling, Adv. Eng. Mater. 14 (2012) 10–19. https://doi.org/10.1002/adem.201100178.

[16] S. Fähler, V.K. Pecharsky, Caloric effects in ferroic materials, MRS Bull. 43 (2018) 264–268. https://doi.org/10.1557/mrs.2018.66.

[17] J.A. Lozano, M.P. Kostow, E. Bru, J.C. De Lima, A.T. Prata, P.A.P. Wendhausen, Porous manganese-based magnetocaloric material for magnetic refrigeration at room temperature, J. Magn. Magn. Mater. 320 (2008) 189–192. https://doi.org/10.1016/j.jmmm.2008.02.044.

[18] J.D. Moore, D. Klemm, D. Lindackers, S. Grasemann, R. Träger, J. Eckert, Selective laser melting of La (Fe , Co , Si) 13 geometries for magnetic refrigeration, J. Appl. Phys. 114 (2013) 1–9. https://doi.org/10.1063/1.4816465.

[19] B. Pulko, J. Tušek, J.D. Moore, B. Weise, K. Skokov, O. Mityashkin, A. Kitanovski, C. Favero, P. Fajfar, O. Gutfleisch, A. Waske, A. Poredoš, Epoxy-bonded La-Fe-Co-Si magnetocaloric plates, J. Magn. Magn. Mater. 375 (2015) 65–73. https://doi.org/10.1016/j.jmmm.2014.08.074.

[20] A. Funk, M. Zeilinger, A. Miehe, D. Sopu, J. Eckert, F. Dötz, A. Waske, MnFePSi-based magnetocaloric packed bed regenerators: Structural details probed by X-ray tomography, Chem. Eng. Sci. 175 (2018) 84–90. https://doi.org/10.1016/j.ces.2017.09.030.

[21] M. Krautz, A. Funk, K.P. Skokov, T. Gottschall, J. Eckert, O. Gutfleisch, A. Waske, A new type of La(Fe,Si)13-based magnetocaloric composite with amorphous metallic matrix, Scr. Mater. 95 (2015) 50–53. https://doi.org/10.1016/j.scriptamat.2014.10.002.

[22] I.A. Radulov, K.P. Skokov, D.Y. Karpenkov, T. Gottschall, O. Gutfleisch, On the preparation of La(Fe,Mn,Si)13Hx polymer-composites with optimized magnetocaloric properties, J. Magn. Magn. Mater. 396 (2015) 228–236. https://doi.org/10.1016/j.jmmm.2015.08.044.

[23] V. Laitinen, A. Sozinov, A. Saren, A. Salminen, K. Ullakko, Laser powder bed fusion of Ni-Mn-Ga magnetic shape memory alloy, Addit. Manuf. 30 (2019) 100891. https://doi.org/10.1016/j.addma.2019.100891.

[24] V. Laitinen, A. Salminen, K. Ullakko, First investigation on processing parameters for laser powder bed fusion of Ni-Mn-Ga magnetic shape memory alloy, J. Laser Appl. 31 (2019) 022303. https://doi.org/10.2351/1.5096108.

[25] F. Nilsén, I.F. Ituarte, M. Salmi, J. Partanen, S.P. Hannula, Effect of process parameters on non-modulated Ni-Mn-Ga alloy manufactured using powder bed fusion, Addit. Manuf. 28 (2019) 464–474. https://doi.org/10.1016/j.addma.2019.05.029.

[26] A. Mostafaei, P. Rodriguez De Vecchis, E.L. Stevens, M. Chmielus, Sintering regimes and resulting microstructure and properties of binder jet 3D printed Ni-Mn-Ga magnetic shape memory alloys, Acta Mater. 154 (2018) 355–364.

[27] A. Mostafaei, K.A. Kimes, E.L. Stevens, J. Toman, Y.L. Krimer, K. Ullakko, M. Chmielus, Microstructural evolution and magnetic properties of binder jet additive manufactured Ni-

Mn-Ga magnetic shape memory alloy foam, Acta Mater. 131 (2017) 482–490. https://doi.org/10.1016/j.actamat.2017.04.010.

[28] M.P. Caputo, C. V. Solomon, A facile method for producing porous parts with complex geometries from ferromagnetic Ni-Mn-Ga shape memory alloys, Mater. Lett. 200 (2017) 87–89.

[29] M.P. Caputo, A.E. Berkowitz, A. Armstrong, P. Müllner, C.V. Solomon, 4D printing of net shape parts made from Ni-Mn-Ga magnetic shape-memory alloys, Addit. Manuf. 21 (2018) 579–588. https://doi.org/10.1016/j.addma.2018.03.028.

[30] S.L. Taylor, R.N. Shah, D.C. Dunand, Ni-Mn-Ga micro-trusses via sintering of 3D-printed inks containing elemental powders, Acta Mater. 143 (2018) 20–29.

[31] E. Stevens, K. Kimes, V. Chernenko, P. Lazpita, A. Wojcik, W. Maziarz, M. Chmielus, Direct laser deposition and homogenization of Ni-Co-Mn-Sn magnetoaloric materials, Microsc. Microanal. 24 (2018) 956–957.

[32] E. Stevens, D. Salazar, K. Kimes, R.R. de Vecchis, V. Chernenko, M. Chmielus, Additive Manufacturing of Ni-Mn-Cu-Ga: Influence of Sintering Temperature on Magnetocaloric Effect and Microstructure, Microsc. Microanal. 25 (2019) 2578–2579. https://doi.org/10.1017/S143192761901362X.

[33] W.J. Feng, L. Zuo, Y.B. Li, Y.D. Wang, M. Gao, G.L. Fang, Abnormal e/a-dependence of TM and large inverse magnetocaloric effect in Ni49-xCuxMn39Sb12 alloys, Mater. Sci. Eng. B Solid-State Mater. Adv. Technol. 176 (2011) 621–625. https://doi.org/10.1016/j.mseb.2011.02.003.

[34] J. Marcos, L. Mañosa, A. Planes, F. Casanova, X. Batlle, A. Labarta, Multiscale origin of the magnetocaloric effect in Ni-Mn-Ga shape-memory alloys, Phys. Rev. B. 68 (2003) 094401. https://doi.org/10.1103/PhysRevB.68.094401.

[35] A. Mostafaei, E.L. Stevens, E.T. Hughes, S.D. Biery, C. Hilla, M. Chmielus, Powder bed binder jet printed alloy 625: densification, microstructure and mechanical properties, Mater. Des. 108 (2016) 126–135.

[36] A. Mostafaei, P. Rodriguez De Vecchis, E.L. Stevens, M. Chmielus, Sintering regimes and resulting microstructure and properties of binder jet 3D printed Ni-Mn-Ga magnetic shape memory alloys, Acta Mater. 154 (2018) 355–364. https://doi.org/https://doi.org/10.1016/j.actamat.2018.05.047.

[37] C.A. Schneider, W.S. Rasband, K.W. Eliceiri, NIH Image to ImageJ: 25 years of image analysis, Nat. Methods. 9 (2012) 671–675.

[38] J. Rodríguez-Carvajal, Recent advances in magnetic structure determination by neutron powder diffraction, Phys. B Condens. Matter. 192 (1993) 55–69. https://doi.org/10.1016/0921-4526(93)90108-I.

[39] D. Salazar-Jaramillo, P. Álvarez-Alonso, P. Lázpita, J.L. Sánchez-Llamazares, P. Gorria, J.A. Blanco, V.A. Chernenko, Magnetocaloric Effect in Specially Designed Materials, in: Magn. Nanostructured Mater. From Lab to Fab, Elsevier, Amsterdam, 2018: pp. 199–244.

[40] P. Álvarez-Alonso, J. López-García, G. Daniel-Perez, D. Salazar, P. Lázpita, J.P. Camarillo, H. Flores-Zuñiga, D. Rios-Jara, J.L. Sánchez-Llamazares, V.A. Chernenko, Simple Set-Up

for Adiabatic Measurements of Magnetocaloric Effect, Key Eng. Mater. 644 (2015) 215–218. https://doi.org/10.4028/www.scientific.net/KEM.644.215.

[41] J. Svoboda, H. Riedel, H. Zipse, Equilibrium pore surfaces, sintering stresses and constitutive equations for the intermediate and late stages of sintering—I. computation of equilibrium surfaces, Acta Metall. Mater. 42 (1994) 435–443. https://doi.org/10.1016/0956-7151(94)90498-7.

[42] G. Okuma, D. Kadowaki, T. Hondo, A. Sato, S. Tanaka, F. Wakai, Computation of sintering stress and bulk viscosity from microtomographic images in viscous sintering of glass particles, J. Am. Ceram. Soc. 100 (2017) 867–875. https://doi.org/10.1111/jace.14609.

[43] P.-P. Li, J.-M. Wang, C.-B. Jiang, Martensitic transformation in Cu-doped NiMnGa magnetic shape memory alloys, Chinese Phys. B. 20 (2011) 028104. https://doi.org/10.1088/1674-1056/20/2/028104.

[44] S.K. Sarkar, Sarita, P.D. Babu, A. Biswas, V. Siruguri, M. Krishnan, Giant magnetocaloric effect from reverse martensitic transformation in Ni–Mn–Ga–Cu ferromagnetic shape memory alloys, J. Alloys Compd. 670 (2016) 281–288. https://doi.org/10.1016/j.jallcom.2016.02.039.

[45] S. Roy, E. Blackburn, S.M. Valvidares, M.R. Fitzsimmons, S.C. Vogel, M. Khan, I. Dubenko, S. Stadler, N. Ali, S.K. Sinha, J.B. Kortright, Delocalization and hybridization enhance the magnetocaloric effect in Cu-doped Ni2 MnGa, Phys. Rev. B - Condens. Matter Mater. Phys. 79 (2009) 1–5. https://doi.org/10.1103/PhysRevB.79.235127.

[46] A. Smith, C.R.H. Bahl, R. Bjork, K. Engelbrecht, K.K. Nielsen, N. Pryds, Materials challenges for high performance magnetocaloric refrigeration devices, Adv. Energy Mater. 2 (2012) 1288–1318. https://doi.org/10.1002/aenm.201200167.

[47] R. Bjørk, C.R.H. Bahl, A. Smith, N. Pryds, Review and comparison of magnet designs for magnetic refrigeration, Int. J. Refrig. 33 (2010) 437–448. https://doi.org/10.1016/j.ijrefrig.2009.12.012.

[48] R. Wroblewski, K. Sielicki, M. Leonowicz, Magnetocaloric properties of Ni49.9Mn19.6Cu5.7Ga24.8single crystal processed by Bridgman method with stationary crucible, Mater. Lett. 218 (2018) 83–85. https://doi.org/10.1016/j.matlet.2018.01.174.

[49] Z. Li, Z. Li, B. Yang, Y. Zhang, C. Esling, X. Zhao, L. Zuo, Large low-field magnetocaloric effect in a directionally solidified Ni50Mn18Cu7Ga25 alloy, Intermetallics. 88 (2017) 31–35. https://doi.org/10.1016/j.intermet.2017.05.002.

[50] N. Zou, Z. Li, Y. Zhang, C.F. Sánchez-Valdés, J.L. Sánchez Llamazares, C. Esling, B. Yang, X. Zhao, L. Zuo, Transformation process dependent magnetocaloric properties of annealed Ni 50 Mn 18 Cu 7 Ga 25 ribbons, J. Alloys Compd. 698 (2017) 731–738. https://doi.org/10.1016/j.jallcom.2016.12.178.

[51] P. La Roca, L. Isola, P. Vermaut, J. Malarría, Relationship between grain size and thermal hysteresis of martensitic transformations in Cu-based shape memory alloys, Scr. Mater. 135 (2017) 5–9. https://doi.org/10.1016/j.scriptamat.2017.03.016.

[52] V. V. Kokorin, L.E. Kozlova, A.N. Titenko, Temperature hysteresis of martensite transformation in aging Cu-Mn-Al alloy, Scr. Mater. 47 (2002) 499–502.

https://doi.org/10.1016/S1359-6462(02)00136-7.

[53] P.K. Gokuldoss, S. Kolla, J. Eckert, Additive manufacturing processes: Selective laser melting, electron beam melting and binder jetting-selection guidelines, Materials (Basel). 10 (2017).

[54] O.A. Likhachev, Y.M. Koval, Hysteresis phenomena and their modelling in martensitic transformation thermodynamics, Usp. Fiz. Met. 16 (2015) 23–34. https://doi.org/10.15407/ufm.16.01.023.

[55] H. Yan, Crystal structure, martensitic transformation crystallography, mechanical and magnetocaloric performance of Ni(Co)MnIn multifunctional alloys, University of Lorraine and Northeastern University, 2016. http://www.theses.fr/2016LORR0105/document.

[56] I. Ruiz-Larrea, A. López-Echarri, J.F. Gómez-Cortés, M.L. Nó, D.W. Brown, L. Balogh, T. Breczewski, J. San Juan, Strain relaxation in Cu-Al-Ni shape memory alloys studied by in situ neutron diffraction experiments, J. Appl. Phys. 125 (2019). https://doi.org/10.1063/1.5049216.

[57] K.P. Skokov, D.Y. Karpenkov, M.D. Kuz'min, I.A. Radulov, T. Gottschall, B. Kaeswurm, M. Fries, O. Gutfleisch, Heat exchangers made of polymer-bonded La(Fe,Si)13, J. Appl. Phys. 115 (2014) 2012–2015. https://doi.org/10.1063/1.4868707.

[58] S. Stadler, M. Khan, J. Mitchell, N. Ali, A.M. Gomes, I. Dubenko, A.Y. Takeuchi, A.P. Guimarães, Magnetocaloric properties of Ni 2Mn1-xCuxGa, Appl. Phys. Lett. 88 (2006). https://doi.org/10.1063/1.2202751.

[59] V. Sokolovskiy, V. Buchelnikov, K. Skokov, O. Gutfleisch, D. Karpenkov, Y. Koshkid'Ko, H. Miki, I. Dubenko, N. Ali, S. Stadler, V. Khovaylo, Magnetocaloric and magnetic properties of Ni2Mn1-xCuxGa Heusler alloys: An insight from the direct measurements and ab initio and Monte Carlo calculations, J. Appl. Phys. 114 (2013). https://doi.org/10.1063/1.4826366.

[60] A. Gebert, S. Roth, S. Oswald, L. Schultz, Passivity of polycrystalline NiMnGa alloys for magnetic shape memory applications, Corros. Sci. 51 (2009) 1163–1171. https://doi.org/10.1016/j.corsci.2009.02.016.

[61] M. Suzuki, M. Ohtsuka, M. Matsumoto, Y. Murakami, D. Shindo, K. Itagaki, Effect of aging time on shape memory properties of sputtered Ni-rich Ni2MnGa alloy films, Mater. Trans. 43 (2002) 861–866. https://doi.org/10.2320/matertrans.43.861.

[62] N. Jetta, N. Ozdemir, S. Rios, D. Bufford, I. Karaman, X. Zhang, Phase transformations in sputtered Ni–Mn–Ga magnetic shape memory alloy thin films, Thin Solid Films. 520 (2012) 3433–3439. https://doi.org/10.1016/j.tsf.2011.12.029.

[63] M. Chmielus, C. Witherspoon, R.C. Wimpory, A. Paulke, A. Hilger, X. Zhang, D.C. Dunand, P. Müllner, Magnetic-field-induced recovery strain in polycrystalline Ni-Mn-Ga foam, J. Appl. Phys. 108 (2010) 1–7.